Accepted Manuscript

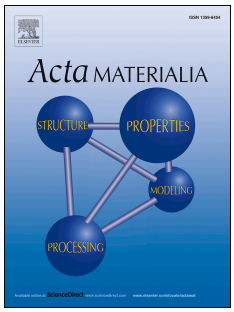

In situ, 3D characterization of the deformation mechanics of a superelastic NiTi shape memory alloy single crystal under multiscale constraint

Harshad M. Paranjape, Partha P. Paul, Behnam Amin-Ahmadi, Hemant Sharma, Darren Dale, J.Y. Peter Ko, Yury I. Chumlyakov, L. Catherine Brinson, Aaron P. Stebner

PII: S1359-6454(17)30969-2

DOI: 10.1016/j.actamat.2017.11.026

Reference: AM 14197

To appear in: *Acta Materialia*

Received Date: 26 August 2017

Revised Date: 10 November 2017

Accepted Date: 13 November 2017

Please cite this article as: H.M. Paranjape, P.P. Paul, B. Amin-Ahmadi, H. Sharma, D. Dale, J.Y. Peter Ko, Y.I. Chumlyakov, L. Catherine Brinson, A.P. Stebner, In situ, 3D characterization of the deformation mechanics of a superelastic NiTi shape memory alloy single crystal under multiscale constraint, *Acta Materialia* (2017), doi: 10.1016/j.actamat.2017.11.026.

In Situ, 3D Characterization of the Deformation Mechanics of a Superelastic NiTi Shape Memory Alloy Single Crystal Under Multiscale Constraint

Harshad M. Paranjape[a,b,*], Partha P. Paul[b], Behnam Amin-Ahmadi[a], Hemant Sharma[c], Darren Dale[d], J. Y. Peter Ko[d], Yury I. Chumlyakov[e], L. Catherine Brinson[b], Aaron P. Stebner[a]

[a] *Mechanical Engineering, Colorado School of Mines, Golden, CO 80401, USA*
[b] *Mechanical Engineering, Northwestern University, Evanston, IL 60208, USA*
[c] *Advanced Photon Source, Argonne National Laboratory, Argonne, IL 60439, USA*
[d] *Cornell High Energy Synchrotron Source, Cornell University, Ithaca NY 14853*
[e] *Siberian Physical Technical Institute, Tomsk 634050, Russia*

Abstract

Microstructural elements in NiTi shape memory alloys (SMAs) – precipitates, phase boundaries, inclusions, grain boundaries – can be viewed as sources of multiscale constraint that influence their deformation response. We characterized in situ, and in 3D, the deformation and the evolution of microstructure during a tension test in a superelastic NiTi specimen containing some of these sources of constraint. The method used was far-field high-energy X-ray diffraction microscopy (ff-HEDM), complemented by electron microscopy. We simulated the local stress state in the specimen using a microstructural model informed by the experimental data. Using these combined microstructure, deformation, and stress data, we report three phenomena, and relate them to specific sources of constraint. During initial elastic loading, axial lattice strain in austenite increased monotonically. On partial stress-induced phase transformation to martensite, the stress redistributed to both phases leading to a stress relaxation in austenite. The specimen contained a dense distribution of inclusions, which led to the activation of martensite habit plane variants that produce less than theoretical maximum transformation strain. Large Ni_4Ti_3 precipitates potentially contributed to the poor transformation response. Under load, proportional gradients in local rotation and elastic stretch developed in the martensite phase, because of the constraint at phase interfaces. This combined ff-HEDM, electron microscopy, microstructural simulation toolbox

*Corresponding Author
Email address: hparanja@mines.edu (Harshad M. Paranjape)

provides a versatile method to understand the effect of constraint on inelastic deformation in other alloys with hierarchical microstructure.

Keywords: phase transformation (A), microstructures (A), finite elements (C), X-ray diffraction

1. Introduction

Thermoelastic shape memory alloys (SMAs) exhibit two phenomena of practical use – shape memory effect and superelasticity – due to the occurrence of thermally-driven or stress-driven martensitic phase transformation between a high crystal symmetry austenite phase and a low crystal symmetry martensite phase. The martensite phase typically forms a twinned microstructure. Depending on the temperature and stress, the two phases can coexist. The austenite-martensite phases, together with other microstructural elements such as precipitates, inclusions, and grain boundaries, form a hierarchy of microstructure.

The elements of the hierarchical microstructure in SMAs can be viewed as sources of constraint, since these elements influence the deformation in specific ways. The microstructure of nickel-titanium (NiTi) SMAs can consist of elements spanning a nanometer-to-millimeter size range, including nanoscale Ni_4Ti_3 precipitates, austenite-martensite interfaces, grain boundaries, micron-scale TiC and TiO_2 inclusions. Smaller ($< 30\,\text{nm}$), coherent Ni_4Ti_3 precipitates can suppress dislocation motion and stabilize martensite due to local stress fields [1, 2], induce R-phase [3, 4], and reduce local apparent transformation strains [5]. Constraint due to compatibility requirement at the austenite-twinned-martensite interfaces can lead to local stress concentrations, which can induce slip in austenite [6–9]. Transformation is constrained at the grain boundaries, and the grain-neighbor interactions can lead to grain-scale transformation heterogeneity [10] and activation of martensite habit plane variants (HPVs) that produce less-than-ideal transformation strain [11]. Various inclusions in NiTi are typically stiffer than the matrix [12], and thus may act as sites for micro-crack initiation [13]. Larger, artificially introduced TiC inclusions, in contrast, may increase the threshold stress for fatigue crack initiation [14].

While a macroscopic, volume-averaged understanding of these constraint-influenced deformation phenomena is often adequate for choosing SMA compositions and processing methods for engineering applications, a detailed microstructure-scale characterization can provide a more fundamental mechanistic understanding and improve our ability to predict component lifetimes and failure modes. Some of the past characterization studies were able to

obtain such mechanistic understanding by incorporating micromechanical modeling. For example, Gao et al. [15] used phase-field modeling informed by transmission electron microscopy (TEM) to determine the stress field around nanoscale precipitates in NiTiPt SMAs, and then demonstrated that the stress field in certain locations could assist the martensitic transformation. Various researchers used crystallographic calculations and microstructural simulations of the stress field at the austenite-martensite interface in stressed NiTi to show that the local stress concentrations at the interface can induce slip in austenite, and with the knowledge of martensite microstructure formed, the slip systems activated in austenite can be predicted [6–8]. Ueland and Schuh [16] used in situ scanning electron microscopy (SEM) together with microstructural simulations to show that the stress-induced martensite microstructure is more complex at grain boundaries and triple-junctions in copper-aluminum-nickel SMA polycrystal wires compared to the martensite microstructure in oligocrystalline wires with bamboo-type grain morphology. They connected this information to superior cyclic superelastic response shown by bamboo-type wires compared to wires containing grain triple junctions. At the grain scale, Kimiecik et al. [17] combined in situ surface strain measurements using digital image correlation (DIC) in superelastic NiTi with crystallographic calculations to show that martensite HPVs with variant ratios deviating from the value needed to form a compatible austenite-martensite interface may form under load. They connected the formation of this incompatible interface to irrecoverable strain accumulation on cyclic loading and resultant gradual loss in the SMA work output.

The characterization schemes in the efforts reviewed above are either ex situ, or provide deformation information on the surface, or result in specimen damage during measurement. Recent developments in X-ray diffraction-based, 3D, in situ characterization techniques provide an ability to quantify both deformation and microstructure evolution without damaging the specimen during measurement. One such technique, far-field high energy diffraction microscopy (ff-HEDM) can furnish grain-scale information in terms of grain center of mass, grain volume, grain-averaged crystal orientation, and lattice strain tensor as a specimen is thermo-mechanically loaded. The grain-scale information from ff-HEDM can be coupled with microstructural modeling methods such as crystal plasticity. The combination of ff-HEDM and microstructural modeling has been extensively used to relate deformation phenomena in materials exhibiting plasticity and twinning [18–26]. Few studies related to SMAs have used this technique. Berveiller et al. [27] used ff-HEDM to show that grains in CuAlBe SMA undergo reversible rotations of approximately 1° during superelastic loading. Sedmak et al.

[28] obtained the austenite grain structure at a stationary austenite-martensite interface in a stressed superelastic NiTi wire and showed that the phase interface is cone-shaped and a stress-concentration zone exists at the cone tip that drives the propagation of the interface, leading to sustained localized deformation in wires. Paranjape et al. [10] obtained ff-HEDM measurement of grain structure and lattice strain distribution before and after cyclically loading a superelastic NiTi specimen and showed that a deformation heterogeneity develops between the constrained grains in the specimen interior vs. relatively unconstrained grains at the free surface. They also used this information in an anisotropic elastic microstructural model and demonstrated that a similar heterogeneity in deformation develops between the interior of the grain and the grain boundary during subsequent loading.

In this work we present an ff-HEDM- and modeling-based study of the deformation phenomena in a superelastic NiTi SMA single crystal and connect those phenomena to three sources of microstructural constraint: inclusions, precipitates, and phase boundaries. The single crystal contains subgrains that are distinguishable in the ff-HEDM measurements. However, they are separated by low-angle grain boundaries and thus we will refer to this material as single crystal. Information on the microstructure of both austenite and martensite phases, its evolution during loading, and the evolution of deformation is obtained using ff-HEDM. Using microstructural simulation informed by the characterization data, the local stresses are obtained. The details of the characterization and modeling scheme are provided in Section 2. Using these combined microstructure, deformation, and stress data, we present results in Section 3 that demonstrate that the phase transformation is constrained in terms of the volume fraction of austenite transformed and in terms of the martensite HPVs activated. Both austenite and martensite share stress at the peak load, and more specifically, systematic deformation gradients exist is the martensite phase. In Section 4, we discuss the connection between these results and the constraint exerted by inclusions, precipitates, and phase boundaries.

2. Materials and Methods

2.1. Material and Specimen Preparation

A NiTi single crystal was grown using a modified Bridgman technique. The nominal composition of the material was Ti-50.7at.%Ni. Information on the transformation temperatures obtained from differential scanning calorimetry (DSC), initial phase composition, and subgrain structure is reported in the Results section. A dogbone specimen as shown

in Figure 1(a) with a 1 mm × 1 mm × 1 mm gage was machined using electrical discharge machining (EDM).

2.2. Far-field High-Energy Diffraction Microscopy Experiment

The specimen was mounted on the RAMS2 load frame [29] at Cornell High Energy Synchrotron Source, station F2. In a room-temperature tension test, it was loaded in displacement control at a rate of 1×10^{-3} mm s^{-1} to a maximum load of 890 N. This loading scheme resulted in an engineering strain rate of 5.7×10^{-5} s^{-1} and a peak engineering stress of 890 MPa. Using the ff-HEDM technique, in situ measurements of the centers of mass, volumes, crystal orientations, and elastic strain tensors of austenite (cubic, B2) grains in the gage of the specimen were obtained at several load steps: ① 0 MPa, ② 78 MPa, ③ 168 MPa, ④ 258 MPa, ⑤ 314 MPa, ⑥ 425 MPa, ⑦ 587 MPa, ⑧ 729 MPa, ⑨ 869 MPa, ⑩ 632 MPa, ⑪ 477 MPa, ⑫ 381 MPa, ⑬ 283 MPa, and ⑭ -53 MPa. Near the peak load (i.e., at steps ⑧, ⑨, ⑩), crystal orientations and elastic strain tensors were also determined in the martensite (monoclinic, B19′) phase.

The experimental procedure for performing ff-HEDM measurements and subsequent data analysis is extensively described in the literature in general [30–35], and specifically for superelastic SMAs [10, 28]. In this experiment, a 2 mm wide and 1 mm tall monochromatic X-ray beam with 61.332 keV energy was used to illuminate the gage of the specimen. At each loading step between ① and ⑭, diffraction patterns were recorded on a GE-41RT area detector [36] by rotating the specimen from 0° to 360° about the loading axis. One diffraction pattern was recorded during each 0.1° rotation. Thus, 3600 patterns were obtained for each load step. The MIDAS ff-HEDM analysis suite was used to analyze the data [33, 34, 37]. The B2 and B19′ phases were analyzed independently for steps ⑧-⑩. The lattice parameters used in these analyses are listed in Supplementary Data Table 1. Some analysis in Section 4 involves simulating ff-HEDM patterns. The diffraction pattern simulation was performed using a custom software program [38] based on the heXRD package [39].

During the tension test, surface strain fields in the center region of one of the faces of the specimen were obtained using the DIC technique [40–42]. The contrasting features of the burn pattern on the specimen surface that result from the EDM process were used for DIC measurements. Images of the specimen surface were taken using a digital camera at approximately 1 s intervals. The images were analyzed using the open-source NCORR software [43] to obtain axial surface strains. From the DIC strain data and the load cell load data, global stress-strain curves were constructed. After the ff-HEDM tension test, the

gage section was cut from the specimen using EDM. The gage was also cleaved along a plane parallel to the loading axis. Two flat surfaces of this section were polished, and SEM images were recorded using a FEI Quanta 600F sFEG ESEM. Transmission electron microscopy (TEM) foils were prepared from these sectioned pieces using a focused ion beam (FIB). To characterize the precipitate morphology in the specimen, bright-field images and selected area electron diffraction (SAED) patterns were obtained along a $(1\,0\,0)_{Ni_4Ti_3}$ zone axis using a Thermo Fisher Scientific (formerly FEI) Talos F200 TEM.

2.3. Crystallographic Calculations

To assess the accuracy of B19′ crystal orientations determined from ff-HEDM, orientations of all correspondence variants (CVs) of B19′ that can form from a given B2 orientation were calculated. For this calculation, a lattice correspondence of $[1\,0\,0]_{\,B2} \leftrightarrow [1\,0\,0]_{\,B19'}$, $[0\,1\,1]_{\,B2} \leftrightarrow [0\,1\,0]_{\,B19'}$ was used [44]. From this lattice correspondence, a map $\boldsymbol{G}$ that rotates the B2 basis ($\boldsymbol{E}_{B2}$) into the B19′ basis ($\boldsymbol{E}_{B19'}$) was obtained such that $\boldsymbol{E}_{B19'} = \boldsymbol{G}\boldsymbol{E}_{B2}$. If $\boldsymbol{C_j}$ is one of the 24 rotations of the cubic point group, then a map taking a B2 orientation to each variant of B19′ can be obtained as $\boldsymbol{C_j}^{\mathrm{T}}\boldsymbol{G}\boldsymbol{C_j}$. Thus all B19′ CV crystal orientations ($\boldsymbol{g}_{B19'j}$) that can originate from a B2 orientation ($\boldsymbol{g}_{B2}$) can be calculated as $\boldsymbol{g}_{B19'j} = \boldsymbol{C_j}^{\mathrm{T}}\boldsymbol{G}\boldsymbol{C_j}\boldsymbol{g}_{B2}$. Note that only 12 B19′ orientations are unique out of 24 obtained in this calculation, since we do not incorporate B19′ symmetry group rotations. This calculation was implemented using the MTex package [45] in Matlab.

The deformation tensor ($\boldsymbol{T}_1$) due to the phase transformation from B2 to one of the variants of B19′ was obtained from the strained lattice parameter of B2 (a_0) and B19′ (a, b, c, β) (values listed in Supplementary Data Table 1), and the lattice correspondence above. The form of $\boldsymbol{T}_1$ is shown below.

$$\boldsymbol{T}_1 = \boldsymbol{E}_{B19'}\boldsymbol{E}_{B2}^{-1} = \begin{bmatrix} a\cos(\beta-\pi/2) & 0 & 0; \\ a/\sqrt{2}\sin(\beta-\pi/2) & b/\sqrt{2} & -c/\sqrt{2}; \\ -a/\sqrt{2}\sin(\beta-\pi/2) & b/\sqrt{2} & c/\sqrt{2} \end{bmatrix} \begin{bmatrix} a_0 & 0 & 0 \\ 0 & a_0 & -a_0 \\ 0 & a_0 & a_0 \end{bmatrix}^{-1} \quad (1)$$

$\boldsymbol{T}_1$ can be decomposed into a unique rotation ($\boldsymbol{R}_1$) and a unique stretch ($\boldsymbol{U}_1$); thus 24 stretch tensors ($\boldsymbol{U_i}$) were obtained using the 24 rotations ($\boldsymbol{C_i}$) in the B2 symmetry group: $\boldsymbol{U_i} = \boldsymbol{C_i}^{\mathrm{T}}\boldsymbol{U}_1\boldsymbol{C_i}$.

B19′ habit plane normal ($\boldsymbol{m_i}$), shear ($\boldsymbol{b_i}$), and twin volume ratio (λ) for each HPV were calculated in the B2 lattice frame using the stretch tensors ($\boldsymbol{U_i}$) by following the

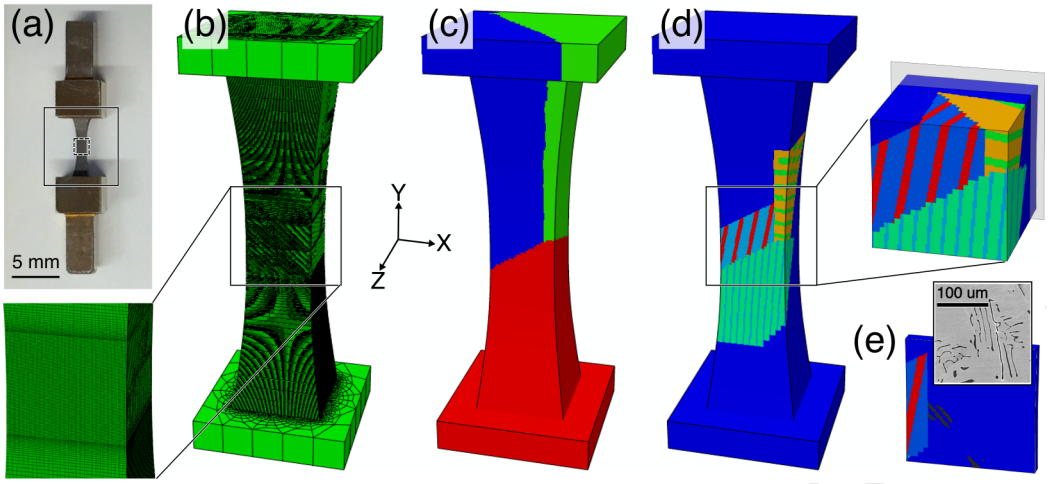

Figure 1: Specimen geometry and the tessellation scheme for microstructural simulations. (a) Specimen with the gage shown by a dashed rectangle and the region modeled in simulations by a solid rectangle. (b) Mesh and an inset showing the mesh density in the gage. (c) Voronoi tessellation to represent B2 grains. (d) Twinned B19′ cells in each B2 grain. Blue color represents B2. The details of the tessellation in the gage section are shown by an inset. (e) A cut of the gage showing modeled inclusion arrays. Inclusions are shown in gray color. Inset shows an SEM micrograph of the inclusion distribution in the specimen.

well-established crystallographic theory of martensite (CTM) [46]. Vectors $\boldsymbol{m_i}$, $\boldsymbol{b_i}$ were transformed to the global frame ($\boldsymbol{m}_i^{\mathrm{g}}$, $\boldsymbol{b}_i^{\mathrm{g}}$) using the B2 crystal orientation ($\boldsymbol{g}_{\mathrm{B2}}$) as follows: $\boldsymbol{b}_i^{\mathrm{g}} = \boldsymbol{g}_{\mathrm{B2}}\boldsymbol{b_i}$ and $\boldsymbol{m}_i^{\mathrm{g}} = \boldsymbol{g}_{\mathrm{B2}}\boldsymbol{m_i}$.

2.4. Multiscale Tessellation from ff-HEDM Data and Microstructural Simulations

From the specimen geometry shown in Figure 1(a), a model was constructed and meshed into $1.4{\times}10^6$ hexahedral elements as shown in Figure 1(b) using Abaqus software [47]. A three-step tessellation scheme was developed to associate each mesh element with a microstructural feature. First, a Voronoi tessellation was generated using the center-of-mass information for B2 grains obtained from the ff-HEDM experiment; thus, each mesh element was assigned a B2 grain whose center of mass was closest to that element. The B2 tessellation is shown in Figure 1(c). Then, in each B2 grain, a cell containing two twinned B19′ CVs in a specific volume ratio was generated. The interface between the B19′ cell and the B2 region of the grain was along the habit plane. The specific CVs that form the twins, their volume ratios, and the habit plane normal were obtained from the ff-HEDM data following the procedure in Section 2.3. A B19′ tessellation using this scheme is shown in Figure 1(d). Finally, cells representing inclusions were introduced as shown by gray regions in Figure 1(e). TiC and TiO_2 inclusion in NiTi typically appear dendrite-shaped, as shown in the inset; thus, the inclusion cells were modeled as arrays of cuboids truncated by an ellipsoid. The size of each inclusion array was randomly selected to be between 50 and 200 µm. The thickness of each cuboid was approximately 10% of the size of the array. On applying this

tessellation scheme, each element in the mesh belonged to one of three phases: B2, B19′, or inclusion.

Microstructural simulations with the goal of obtaining the local stresses were performed in Abaqus software to obtain the local stress evolution in the model under a prescribed strain (i.e., displacement control) and a fixed microstructure generated using the mesh and the tessellation described above. Each element in the mesh was assigned type C3D8 in Abaqus, which resulted in approximately 11.2×10^6 integration points. Based on the phase of a mesh element, an appropriate stiffness tensor was assigned to that element. The stiffness tensor elements for B2, B19′, and inclusion are listed in Supplementary Data Table 2.

An anisotropic elastic and simplified phase transformation constitutive law was implemented to obtain the local stress and deformation distribution. A representative volume element (RVE) consisted of a single crystal of either B2 or inclusion phase. In this study, each element in the finite element mesh was an RVE. Each RVE was initially stress-free ($\boldsymbol{\sigma} = \mathbf{0}$), and had zero martensite volume fraction ($\nu = 0$). At each time increment in this displacement-controlled simulation, a deformation gradient ($\boldsymbol{F}$) was prescribed. The deformation gradient was multiplicatively decomposed into elastic ($\boldsymbol{F}^{\mathrm{e}}$) and phase transformation ($\boldsymbol{F}^{\mathrm{trans}}$) components as

$$\boldsymbol{F} = \boldsymbol{F}^{\mathrm{e}}\boldsymbol{F}^{\mathrm{trans}}. \tag{2}$$

In the mesh elements that are assigned a B19′ phase in the tessellation scheme above, the rate of growth of the martensite volume fraction ($\dot{\nu}_t$) was prescribed using the following law:

$$\dot{\nu}_t = \begin{cases} 0, & \text{if } \sigma_{\mathrm{axial}}^{\mathrm{average}} < 600 \text{ MPa} \\ 5\times10^{-5}\,\mathrm{s}^{-1}, & \text{else.} \end{cases} \tag{3}$$

The value of $5\times10^{-5}\,\mathrm{s}^{-1}$ was determined by trial and error to obtain strains similar to those in the experiment. In the elements belonging to the B2 and inclusion phases, $\dot{\nu}_t = 0$. The evolution of the transformation component of the deformation gradient ($\dot{\boldsymbol{F}}^{\mathrm{trans}}$) was expressed in terms of the velocity gradient ($\boldsymbol{L}^{\mathrm{trans}}$), which, in turn, depended on the deformation gradient ($\boldsymbol{U}_{\boldsymbol{t}}^{\mathrm{trans}}$) produced by the CV t forming in that element as

$$\dot{\boldsymbol{F}}^{\mathrm{trans}} = \boldsymbol{F}^{\mathrm{trans}}\boldsymbol{L}^{\mathrm{trans}}, \quad \boldsymbol{L}^{\mathrm{trans}} = \dot{\nu}_t\boldsymbol{U}_{\boldsymbol{t}}^{\mathrm{trans}}. \tag{4}$$

Since $\dot{\nu}_t = 0$ in the elements of B2 and inclusion type, $\boldsymbol{L}^{\mathrm{trans}}$ did not evolve in those elements.

Cauchy stress ($\boldsymbol{\sigma}$) was calculated from the deformation gradient ($\boldsymbol{F}$) using Hooke's law:

$$\boldsymbol{E} = \frac{1}{2}(\boldsymbol{F}^{\mathrm{e}T}\boldsymbol{F}^{\mathrm{e}} - \boldsymbol{I}), \quad \boldsymbol{T} = \mathcal{C}\boldsymbol{E}, \quad \boldsymbol{\sigma} = \frac{1}{\det \boldsymbol{F}^{e}}\boldsymbol{F}^{e}\boldsymbol{T}\boldsymbol{F}^{T}. \tag{5}$$

Here, $\boldsymbol{E}$ is the Green strain and $\boldsymbol{T}$ is the 2$^{\mathrm{nd}}$ Piola-Kirchhoff stress. The Cauchy stress was then returned to Abaqus.

In B2-type and inclusion-type elements, the stiffness tensor belonging to the B2 and inclusion phases, respectively, was used in Eq. 5. In B19′-type elements, the rule of mixtures was used to determine an effective stiffness: $\mathcal{C} = (1 - \nu_t)\mathcal{C}^{\mathrm{B2}} + \nu_t\mathcal{C}^{\mathrm{B19'}}$.

Stiffness tensor ($\mathcal{C}$), and transformation strain tensors ($\boldsymbol{U}_t^{\mathrm{trans}}$) in the equations above were transformed from the crystal basis to the specimen coordinate system using the crystal orientation of the phase ($\boldsymbol{g}_{\mathrm{B2}}$ or $\boldsymbol{g}_{\mathrm{B19'}}$) to which the mesh element belonged:

$$\mathcal{C} = \boldsymbol{g}\boldsymbol{g}\mathcal{C}^{\mathrm{crystal}}\boldsymbol{g}^{\mathrm{T}}\boldsymbol{g}^{\mathrm{T}}, \quad \boldsymbol{U}_t^{\mathrm{trans}} = \boldsymbol{g}\boldsymbol{U}_t^{\mathrm{trans,\ crystal}}\boldsymbol{g}^{\mathrm{T}} \tag{6}$$

3. Results

3.1. Far-Field High-Energy Diffraction Microscopy Results

The macroscopic axial stress-strain response during the tension test was flag shaped as shown in Figure 2(a). The curve shows hardening immediately after the onset of plateau at ⑦. The stress is calculated from the load cell data and the strain is the mean of the axial strain distribution in the gage measured using DIC. The specimen was in the B2 phase at the start (①) and the end (⑭) of the test as shown by the presence of a B2 peak and the absence of peaks from other phases in the diffraction intensity profile in Figure 2(b). At peak load (⑨), peaks from B19′ phase are visible. The diffraction intensity profile was obtained by summing the area diffraction patterns along the azimuthal direction. See supplementary Data Table 3 for the d-spacing and relative intensities of the peaks shown in Figure 2(b). An onset of localization in the axial strain distribution occurred at step ⑦ as shown in the DIC strain distribution in Figure 2(c). Near peak load, deformation localized in diffuse bands of axial strain $> 4\%$. On unloading, at ⑭, the mean strain was 0.07% and thus some strain was not recovered.

B2 crystal orientations determined from ff-HEDM showed the presence of three grains at ① as in Figure 3(a). The grains were misoriented relative to each other by less than 3° as shown in the inset. Only one of the three grains was identified, after the onset of phase transformation, at loading steps ⑧ to ⑩, as shown in the inverse pole figure for ⑨ in

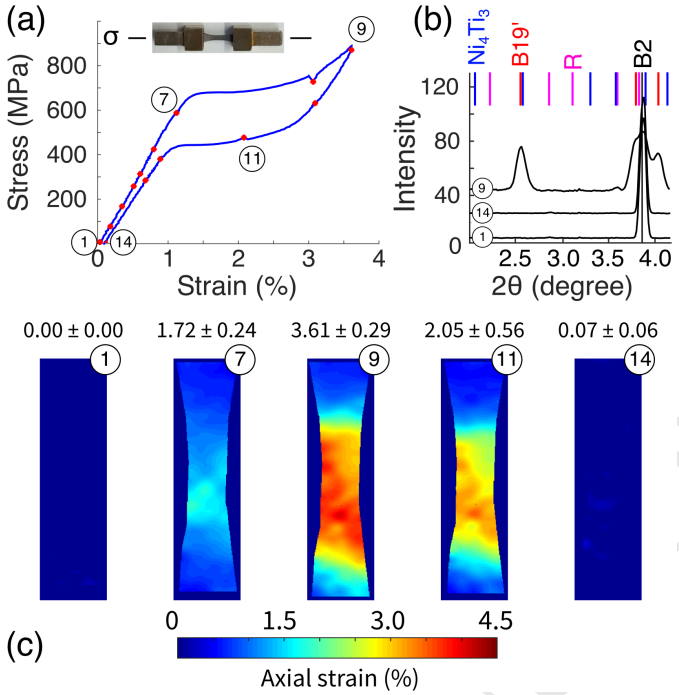

Figure 2: Stress-strain and phase evolution. (a) Macro axial stress vs. axial strain. Ff-HEDM measurements were performed at red points marked ① to ⑭. (b) Diffraction line profile at ①, ⑨, and ⑭. Positions of peaks corresponding to the four common phases in superelastic NiTi are shown. See Supplementary Data Table 3 for d-spacing and relative intensity of these peaks. (c) Evolution of the axial surface strain fields as measured by DIC. Mean ± standard deviation strain are noted above each snapshot.

Figure 3(a). In steps ⑪-⑭, again, all three grains were identified. Four B19′ orientations were identified at step ⑨ as shown in Figure 3(b). The Bragg spots in the raw diffraction data for B19′ at ⑨ were elongated in both radial and azimuthal direction as shown in (c) (see Supplementary Data Figure 1 for the terminology about ff-HEDM spots). The mean radius of the B2 grains, calculated from the grain volumes assuming spherical shape, was constant at approximately 400 µm between steps ① and ⑦ as shown in Figure 3(d). The radius decreased after the onset of transformation at step ⑦, and increased on reverse transformation starting at step ⑩. The mean lattice strain in the axial direction in the B2 grains monotonically increased between steps ① and ⑦ as shown in Figure 3(e). After the onset of phase transformation at step ⑦, B2 relaxed, as seen in terms of a reduction in the lattice strain at steps ⑧-⑩. Then the axial lattice strain in the B2 again increased at step ⑪, before monotonically decreasing to zero on unloading. The axial lattice strain in B19′ phase was measured during steps ⑧-⑩ as shown by the red curve in Figure 3(e). The axial strain in B19′ was higher at peak load (⑨) compared to the strain at ⑧ and ⑩.

The DSC curves for heating and cooling show broad peaks at $A_{\text{peak}} = 299 \pm 1\,\text{K}$ and $M_{\text{peak}} = 296.6 \pm 0.2\,\text{K}$ respectively, both of which are below room temperature (300 K) as

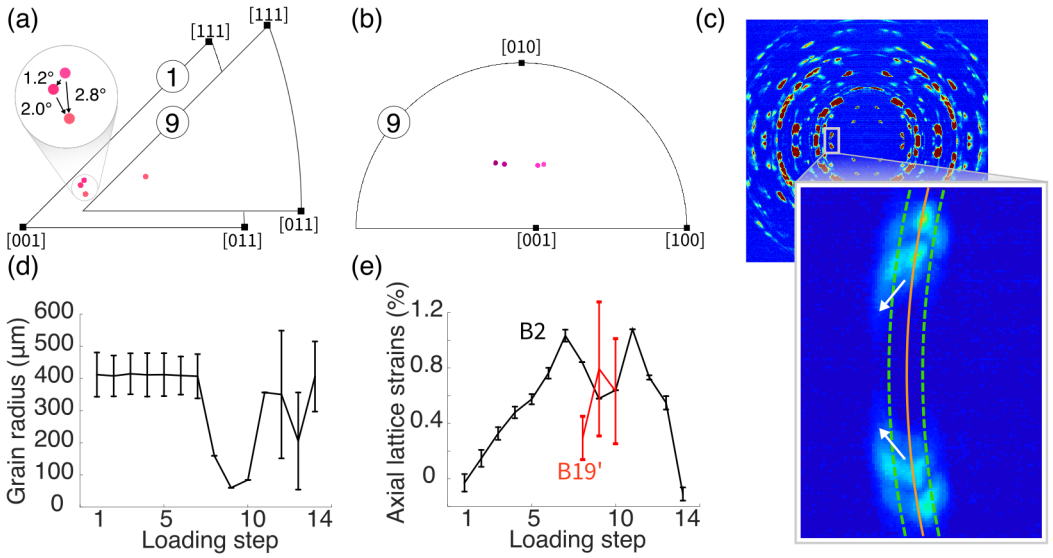

Figure 3: Results from ff-HEDM. (a) B2 orientations at ① reveal that the specimen consisted of three B2 subgrains. The subgrains shared low-angle grain boundaries with pairwise misorientation (shown in inset) of 1°-3°. At ⑨, only one B2 grain was identified. (b) At ⑨ four B19′ orientations were identified. (c) Spots corresponding to B19′ from raw ff-HEDM data were elongated in both radial and azimuthal direction. The B19′ spots are located along the green dashed arc. The spots along the solid orange arc are from B2. (d) The mean B2 grain radius remained constant between steps ① and ⑦, then decreased, and finally increased between steps ⑪ and ⑭. The error bars show the standard deviation for three grains. (e) Mean axial lattice strain in B2 grains (black line) and in B19′ grains (red). Error bars show standard deviation.

shown in Figure 4(a). Similar broad peaks were obtained using two pieces from different locations in the specimen. Because of the broad nature of the peaks, tangent method to estimate the transformation temperatures was not used. SEM analysis of the cleaved specimen gage showed the presence of inclusions seen as dark particle arrays (dendrites) in Figure 4(b). The inclusion size was between 25 and 100 µm. TEM analysis of a foil from the specimen showed the presence of Ni_4Ti_3 precipitates, as seen in Figure 4(c). The zone axis for this measurement was along the [1 0 0] direction of the Ni_4Ti_3 phase. Inset shows a diffraction pattern with spots from the hexagonal lattice of the Ni_4Ti_3 phase. In other locations in the TEM foil (not shown), weak diffraction peaks for R-phase were identified.

3.2. Microstructural Simulation Results

Figure 5(a) shows the simulated axial stress distribution at the macro axial stress of 600 MPa. The stress is concentrated in the gage region. There is no stress heterogeneity at the B2 low-angle grain boundaries (shown by superimposed dashed lines). The macro stress of 600 MPa is at the start of B19′ evolution as specified in Eq. 3. Figure 5(b) shows the axial stress state in the model gage at the macro axial stress of 800 MPa. The corresponding microstructure in the gage is shown in Figure 5(c). The blue regions in (c) are B2, the grey regions are inclusions, and other colors represent B19′ CVs. There is stress heterogeneity in

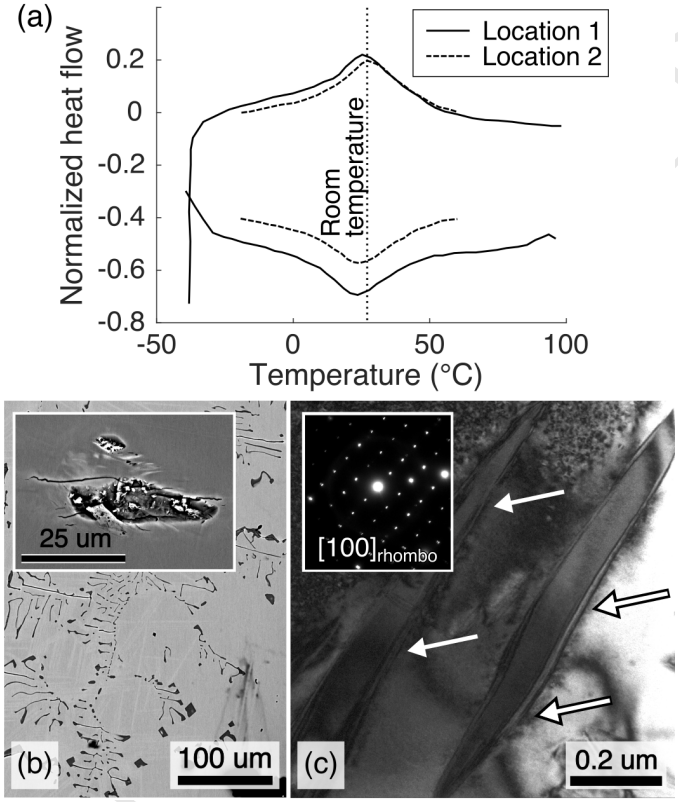

Figure 4: Thermal response and electron microscopy results. (a) Differential scanning calorimetry (DSC) curves for pieces extracted from two locations in the specimen show broad peaks. (b) Scanning electron microscopy (SEM) image shows a distribution of inclusion arrays (dendrites). Inset shows closeup of a single fractured inclusion. (c) Conventional bright field TEM micrograph showing the large Ni_4Ti_3 precipitates (shown by arrows) and corresponding selected area diffraction pattern from the precipitate (inset). Diffraction pattern is taken along $[1\,0\,0]_{\text{rhombohedral}}$ zone axis of the Ni_4Ti_3 precipitates.

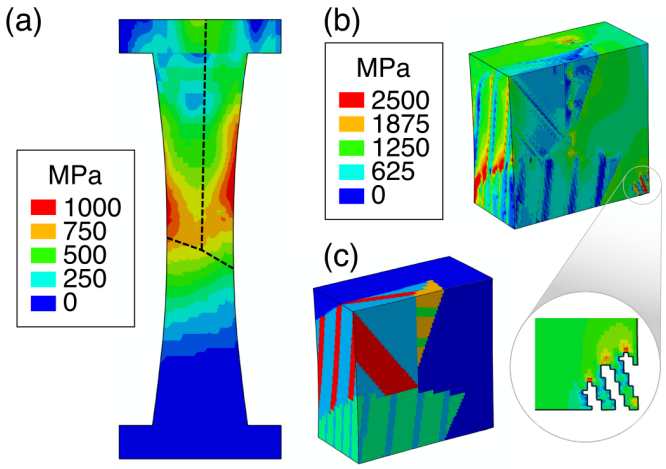

Figure 5: Microstructural simulation results. (a) Axial stress at 600 MPa macro stress. B2 low-angle grain boundaries are shown by dashed lines. (b) A section of the gage showing details of local stress at 800 MPa macro stress. The inset shows the heterogeneous axial stress around an inclusion array. The inclusion itself is not shown. (c) The B19′ microstructure corresponding to the section in (b). Blue regions correspond to B2. Other colors correspond to various B19′ CVs.

different phases. Some phase interfaces show stress concentration in excess of 2 GPa. There is also stress concentration exceeding 1800 MPa around the inclusion, as shown in the inset in Figure 5(b). The region between inclusions is shielded to axial stresses less than 300 MPa.

4. Discussion

The stress-strain response in Figure 2(a) shows hardening right after the onset of phase transformation. The DSC curves in Figure 4(a) show broad peaks, which can be attributed to the presence of inclusions (carbides) in the matrix [48, 49]. SEM results in Figure 4(b) show the presence of inclusion dendrites. These observations together suggest that the phase transformation was constrained. It is known that precipitates [4, 50], phase boundaries [7], and grain boundaries [10] can constrain deformation in NiTi. In this section we discuss the relation between these deformation phenomena and potential sources of microstructural constraint.

4.1. Inefficient B19′ HPVs Activated Under Load

The axial strain distribution in the gage at peak load (⑨) shows a variation between 3 and 4.5%, as plotted in Figure 6(a). Since the axial lattice strain in both the B2 and B19′ phases is available from ff-HEDM as shown in Figure 3, we can calculate the transformation strain as, $\varepsilon^{\text{trans}} = \varepsilon^{\text{total}} - \varepsilon^{\text{lattice}}_{\text{B2}} - \varepsilon^{\text{lattice}}_{\text{B19'}}$. A distribution of the transformation strain at ⑨ is plotted in Figure 6(b). It shows that the $\varepsilon^{\text{trans}}$ varies between 2.75 and 3%.

The theoretical maximum axial transformation strains for HPV formation however, from the strained B2 and B19′ lattice parameters (listed in Supplementary Data Table 1) are of the order of 5.5 to 6%. To perform this calculation, the procedure in Section 2.3 was followed to calculate the transformation stretch matrices ($\boldsymbol{U}$) from the lattice parameters, followed by calculation of habit plane normal and shear direction ($\boldsymbol{m_i}$, $\boldsymbol{b_i}$) for all possible HPVs. The transformation strain matrices for each HPV were determined from $\boldsymbol{m_i}$, $\boldsymbol{b_i}$ and the largest axial transformation strain was determined. This result, together with the analysis of surface strain fields at peak load suggests that inefficient HPVs in terms of axial transformation strain activated in the specimen.

Active B19′ HPVs at peak load determined from the raw ff-HEDM data also suggest that inefficient B19′ HPVs formed. The methodology for determining HPVs from the raw diffraction data is illustrated in Figure 7, and the relevant crystallographic relations are specified in Section 2.3. Using the B2 $\leftrightarrow$ B19′ lattice correspondence, 12 unique B19′ CVs that can form from a B2 orientation were determined, as shown in Figure 7(a). Ff-HEDM spots from each of these B19′ orientations were simulated, and the results were compared with the raw ff-HEDM data at step ⑨. Figure 7(b) shows an example of a good match and a poor match. A match is considered good if the root-mean-squared difference in the centroids of the simulated and actual spots is less than 10 pixels. The CVs determined from one of the B2 grains are shown in Figure 7(c). Once the CVs that are likely to form in each grain were determined, all HPVs that can form from those CVs were determined from CTM [46]. Spots from these HPVs were simulated, considering the small rotations that each CV undergoes at the habit plane. A visual comparison was made between the simulated spots and the raw ff-HEDM data, and the HPV from each B2 grain was picked that furnished the best visual match. The simulated spots from the HPVs determined using this analysis superimposed on the raw ff-HEDM spots are shown in Figure 7(d). A visual comparison between the simulated and actual spots is used rather than a numerical criterion, since a large number of HPV solutions give similar spot patterns; thus, the HPVs determined here are likely to be present in the grains, rather than guaranteed to be present.

The axial transformation strains from the HPVs determined above are 2.02%, 2.62%, and 2.60%, respectively. These strains are smaller than the maximum transformation strains possible for the measured B2/B19′ lattice parameters (= 5.5%-6%). The transformation strains from these HPVs are plotted along with the axial transformation strain distribution in the specimen gage in Figure 6(b). The transformation strains for HPVs compare reasonably

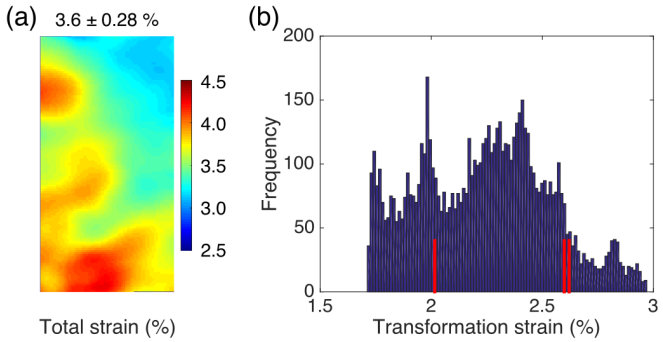

Figure 6: Strain analysis at peak load. (a) Axial total strain ($\varepsilon^{\text{total}}$) in the gage region measured by DIC at peak load. (b) Transformation strain distribution at peak load calculated from the total strain measured by DIC and the lattice strains in B2 and B19′ measured by ff-HEDM: $\varepsilon^{\text{trans}} = \varepsilon^{\text{total}} - \varepsilon^{\text{lattice}}_{\text{B2}} - \varepsilon^{\text{lattice}}_{\text{B19}'}$. The strain corresponding to the HPVs determined in Section 4.2 is shown by red lines.

with the estimated surface transformation strains. While this comparison does not confirm the existence of the specific HPVs, it reinforces the observation that inefficient HPVs formed under load.

Constraint at the grain boundaries between the three B2 grains can cause activation of HPVs that produce less-than-maximum possible transformation strain; however, the misorientation between the grains is less than 2.8°. Constraint at such low-angle grain boundaries would appear unlikely to reduce transformation strain from 5.5% to 2.5%. Results for the microstructural simulations in Figure 5(a), prior to the onset of phase transformation, do not show noticeable stress concentrations at the grain boundaries; thus, the grain boundaries are less likely to be the cause behind the activation of HPVs producing relatively small axial transformation strain. While several efforts in the literature document a deleterious effect of grain boundaries on phase transformation [10, 11, 17, 51], the grain boundaries considered in those works were from typical textured or untextured polycrystals and thus were high-angle boundaries. Here we have subgrain-boundaries that are less than 3° misoriented, and they do not show the same effect.

Stress heterogeneity around the inclusions can be another source of constraint. Figure 4(b) shows a distribution of inclusions in the specimen. The inclusions, typically with a composition of TiC or TiO_2, are stiffer than the B2 matrix, as suggested by their fractured appearance in Figure 4(b, inset). Prior modeling works in the literature have assumed them to have a Young's modulus of approximately 400 GPa [12]; thus, the inclusions can significantly alter the stress around them and the heterogeneous stress distribution around them can activate HPVs different from the rest of the B2 matrix. We quantify the effect of stress state around inclusions on the activation of less efficient HPVs in the next subsection.

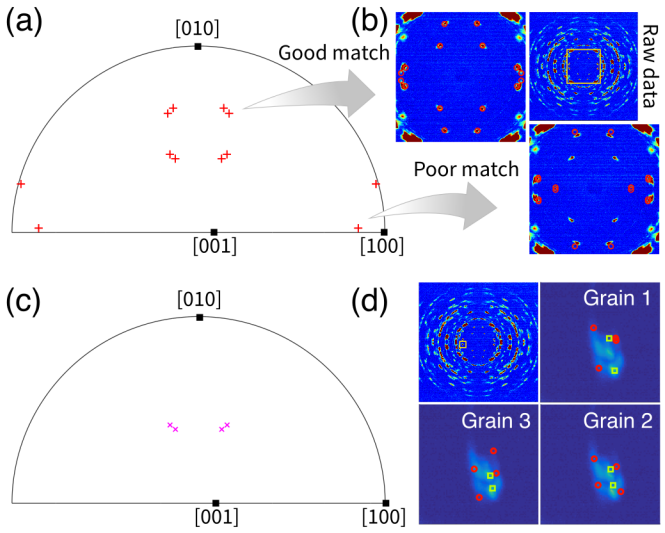

Figure 7: Method for determining B19′ HPVs likely to be present at peak load. (a) Orientations of all B19′ CVs that can form from a B2 orientation are calculated using the orientation relation in Section 2.3. (b) Bragg diffraction spots from each CV orientation are simulated (shown by red circles) and compared with the raw ff-HEDM spot data. An example of a good spot position match and a poor match is shown. In the case of good match, red circles fall on the raw spots. (c) Using a threshold for difference in the simulated and actual spot positions, CVs that are likely to be present are determined. Four CVs shown by magenta × are candidates in one of the B2 grains. (d) All HPVs that can form from the CVs in (c) are calculated following the well-established CTM procedure. Diffraction patterns are simulated from the HPVs and visually compared with the raw spot data. Spots from the HPV in each grain that give the best match are shown. Green squares are the spots from B2 and red circles are the spots from B19′.

4.2. Stress-state Around Inclusions Activated Less-Efficient HPVs

Simulated axial stress distribution at a macro axial stress of 600 MPa shows both stress concentration and stress shielding around an inclusion, as shown in Figure 8(a). Stress in the B2 matrix is shown. With the full simulated stress state known, the HPV likely to form at each point in the mesh can be calculated using the maximum work criterion [52]. The work due to transformation (W_i^{trans}) for an HPV i depends on the local stress ($\boldsymbol{\sigma}$) and the transformation strain ($\boldsymbol{S_i}$):

$$W_i^{\text{trans}} = \boldsymbol{\sigma} : \boldsymbol{S_i}, \quad \boldsymbol{S_i} = \frac{1}{2}(\boldsymbol{b_i} \otimes \boldsymbol{m_i} + \boldsymbol{m_i} \otimes \boldsymbol{b_i}). \tag{7}$$

Vectors $\boldsymbol{b_i}$ and $\boldsymbol{m_i}$ for each HPV are calculated using CTM as outlined in Section 2.3.

Distribution of the axial transformation strain in Figure 8(b) corresponding to the HPV that produced maximum work shows that in some regions the transformation strain is as low as 1.6%. Particularly in the stress-shielded regions between the inclusion particles, the axial transformation strain (1.6-4%) is smaller than the strain in the matrix away from the inclusion (6%). This result shows that the inclusions can act as sites where inefficient B19′ plates can activate. While the region around the inclusion where inefficient plates are likely

to form is relatively small, a dense network of inclusions is present in the specimen as shown in Figure 4. Thus inefficient plates can nucleate at several sites and eventually dominate the transformation response. Such activation of inefficient HPVs from multiple sites suggests interrupted transformation and can also explain the immediate hardening after plateau in Figure 2(a). It is likely that these HPVs forming around inclusions induced slip, which can explain the residual strain on unloading in Figure 2(d). It should be noted that with appropriate sample preparation and experimental setup, theoretical transformation strains can be obtained in SMA single crystals [53, 54].

Similar to inclusions, Ni_4Ti_3 precipitates harbor local heterogeneous stress fields [55, 56]. Inefficient plates can nucleate at these sites, particularly when the precipitates are large as shown in Figure 4(c). However, the aspect ratio of precipitates is similar to that of inclusions, and thus, qualitatively, the effect of stress field around precipitates is likely to be similar to the effect of inclusion stress fields documented above. Quantitative characterization of other subtle effects related to precipitates, such as the effect of Ni content heterogeneity, the effect of specific orientation relationships between the matrix and the precipitate, and the effect of the eigenstrain associated with the precipitate is not accessible to these micro-scale experiments and thus these effects are not the focus of this work. Efstathiou and Sehitoglu [5] also point out that, since Ni_4Ti_3 precipitates do not transform, their presence reduces the B2 volume available for transformation. Thus, the apparent local transformation strain as measured by techniques such as DIC is reduced by a value proportional to the volume fraction of the precipitates. The area fraction of precipitates in Figure 4(c) is low (approximately 23%) and in the raw diffraction data shown in Figure 3(c), the peaks corresponding to the Ni_4Ti_3 phase are not discernible. Thus it is unlikely that in the volumetric sense, Ni_4Ti_3 precipitates reduced the apparent transformation strain by 50% in Figure 6.

Partial transformation from B2 to R-phase can reduce the apparent transformation strain as R-phase produces substantially smaller transformation strains compared to B19′ [57–62]. In this experiment, R-phase peaks were observed at some loading steps (See Supplementary Data Figure 2 for intensities of representative peaks from B2, B19′, and R-phase). However, at peak load (i.e., step ⑨), the intensity of the $(1\,0\,\bar{1}\,1)_{\mathrm{R}}$ peak was not discernible above the background. In the post-mortem TEM analysis, weak spots corresponding to the R phase were observed in certain regions. Thus, it is likely that R-phase formed in measurable quantity as an intermediate in the B2 $\leftrightarrow$ B19′ transformation, but was not measurably present at peak load. The goal of this work is to characterize the martensite microstructure

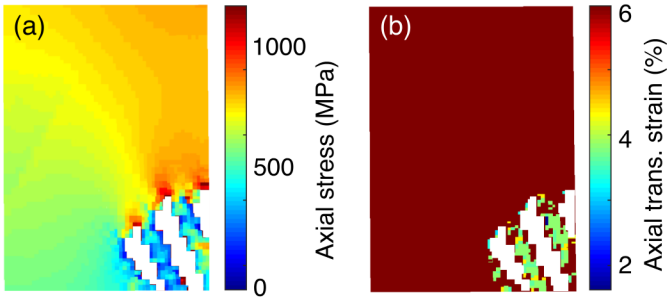

Figure 8: Simulated stress state and predicted B19′ HPV distribution around an inclusion. (a) Axial stress distribution at a macro stress of 800 MPa. (b) Theoretical axial transformation strain for the preferred HPV at each point based on the maximum work criterion.

at peak load and relate that to the other microstructural features present, thus formation of R-phase is not discussed.

4.3. Proportional Gradients in Rotation and Elastic Strain Existed in B19′

The Bragg spots corresponding to B19′ phase in Figure 3(c) are elongated in both radial and azimuthal directions (see Supplementary Data Figure 1 for the terminology related to ff-HEDM spots). Elongation in the radial direction indicates the presence of a lattice strain gradient. Spot elongation in the azimuthal direction indicates the presence of an orientation spread. Since the spot elongation in the radial and azimuthal directions in Figure 3(c) is correlated, rather than random, we hypothesize that proportional gradients in lattice rotation and elastic strain exist in the B19′ phase under load.

To test this hypothesis, we examine the simulated deformation in the B19′ twin bands. The elastic deformation gradient ($\boldsymbol{F}^{\mathrm{e}}$) returned from the simulation can be decomposed into a rotation ($\boldsymbol{R}^{\mathrm{e}}$) and a stretch ($\boldsymbol{U}^{\mathrm{e}}$) as $\boldsymbol{F}^{\mathrm{e}} = \boldsymbol{R}^{\mathrm{e}}\boldsymbol{U}^{\mathrm{e}}$. Note that $\boldsymbol{U}^{\mathrm{e}}$ and elastic strain ($\boldsymbol{\varepsilon}^{\mathrm{e}}$) are related as: $\boldsymbol{\varepsilon}^{\mathrm{e}} = 1/2(\boldsymbol{U}^{\mathrm{e}T}\boldsymbol{U}^{\mathrm{e}} - \boldsymbol{I})$. Figure 9(a) shows the local rotation angle calculated from $\boldsymbol{R}^{\mathrm{e}}$ at a macro axial stress of 800 MPa. Rotations are larger near B2-B19′ habit planes and B19′-B19′ interfaces compared to those in the interior regions of the B2 phase and some B19′ variants. Similar to rotation angle, gradients in the axial component of elastic stretch ($\boldsymbol{U}^{\mathrm{e}}_{\boldsymbol{22}}$) exist in B19′ as shown in Figure 9(b). The gradients in both rotation and elastic stretch are more prominent along a path PQ traversing from the interior of a B19′ twin to an interface. The gradients along PQ in rotation and stretch are shown in Figure 9(c, d). In going from P to Q (i.e., toward an interface), the elastic stretch decreased and rotation angle increased. This can be viewed as a result of the constraint acting at B19′-B19′ interfaces. These data prove our hypothesis that proportional gradients in rotation and elastic deformation exist in B19′.

To visually verify that the proportional gradients in rotation and stretch in B19′ can lead

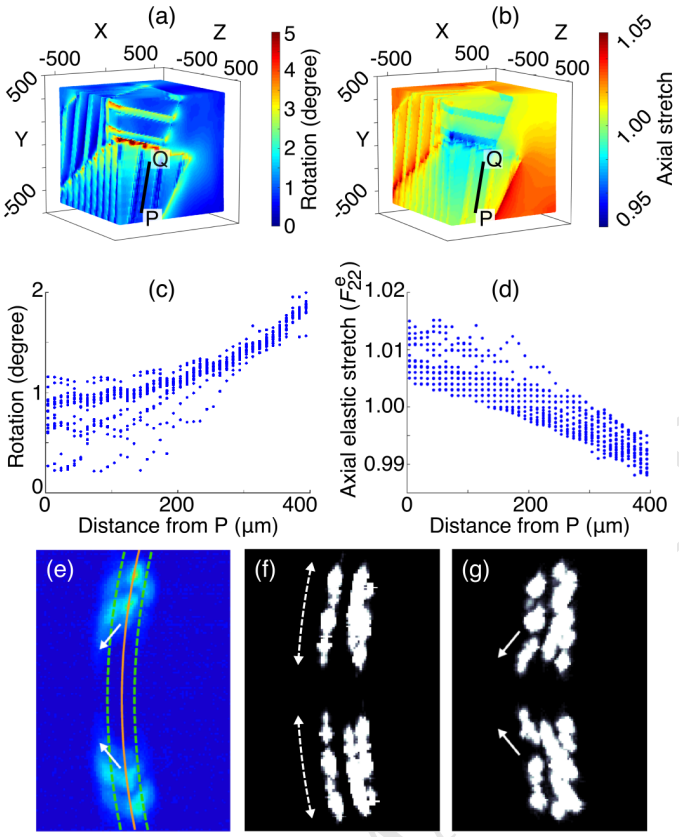

Figure 9: Local elastic stretch and rotation in the B19′ phase vary systematically in the twin bands as a function of the distance from the nearest phase interface. (a) Rotation at 800 MPa macro axial stress in the simulations. (b) Axial elastic stretch at the same macro stress. (c) Rotation along a path PQ in one martensite CV. (d) Axial elastic stretch along the same path PQ. (e) Experimental spot patterns at peak stress. Austenite spots are along the solid orange arc. Martensite spots are along the dashed green arcs. Martensite spots show systematic elongation in both radial and azimuthal directions. (f) Simulated spot patterns using only the rotation information from the microstructural simulation at 800 MPa macro axial stress show azimuthal elongation (dashed arrow), but not radial elongation. (g) Simulated spots show both radial and azimuthal spread similar to (e) when both rotation and elastic stretch from the microstructural simulations are considered.

to the specific spots shapes, we simulate the ff-HEDM spot patterns using the orientation data for B2, B19′, and the deformation data discussed above. Figure 9(e) shows the experimental spot shape elongation. Figure 9(f) shows the simulated patterns using only rotations. The spots show azimuthal spread but no radial spread. Figure 9(g) shows simulated spots using both rotation and elastic stretch. In this case, both radial and azimuthal spreads are present and they are qualitatively similar to (e).

5. Conclusions

We used an in situ, 3D, non-destructive characterization technique – far-field high-energy X-ray diffraction microscopy (ff-HEDM) – to quantify the evolution in deformation and microstructure in both B2 and B19′ phases in a superelastic NiTi single crystal containing

subgrains that was loaded in tension. From these experimental microstructure data, we are able to determine the B19′ correspondence variants and habit plane variants that are likely to have formed under load. We performed simulations informed by the experimentally characterized microstructure to obtain local stress state under load. From this combined microstructure, deformation, and stress information, we are able to demonstrate that

1. Inefficient B19′ HPVs in terms of axial transformation strain formed under stress and produced 50% axial transformation strain compared to the theoretical maximum.
2. Inclusions acted as sources of constraint and the local stress heterogeneity around the inclusions activated less efficient HPVs. Precipitates potentially contributed to this phenomenon.
3. B2-B19′ and B19′-B19′ interfaces acted as another source of constraint and led to proportional gradients in rotation and elastic stretch in B19′ phase.
4. Small-angle grain boundaries in the single crystal did not noticeably constrain the deformation.

The mechanistic understanding from combined 3D experimental-modeling approaches such as this can be used to either develop material processes that mitigate constraint (e.g., mitigation of grain boundary constraint by precipitation of a ductile phase at the boundaries [63]), or to engineer these sources of constraint to improve mechanical properties [64]. This coupled approach can be used to study the effect of constraint on the deformation in other inelastically deforming materials with hierarchical microstructures: titanium alloys, steels, and magnesium alloys.

Acknowledgement

HMP, PPP, and LCB acknowledge financial support from the US Department of Energy, Office of Basic Energy Sciences (grant no. DE-SC0010594). BA was supported by the Confluent Medical Technologies Postdoctoral Fellowship. HS's work at the Advanced Photon Source was supported by the US Department of Energy, Office of Science, Office of Basic Energy Sciences, under contract no. DE-AC02-06CH11357. APS was supported by NSF-Career award no. 1454668. The work of YC was carried out with financial support from the Ministry of Science and Education of Russian Federation (State Task no. 16.6554.2017/6.7). This work used the Extreme Science and Engineering Discovery Environment (XSEDE), which is supported by National Science Foundation grant number ACI-1053575. This work is based

upon research conducted at the Cornell High Energy Synchrotron Source (CHESS) which is supported by the National Science Foundation under award DMR-1332208. Scanning electron microscopy work was performed at MatCI (funded by NSF DMR-1121262) and NUANCE (funded by NSF ECCS-1542205) facilities at Northwestern University. Authors thank Dr. Joel V. Bernier (Lawrence Livermore National Laboratory) for helpful discussions related to ff-HEDM data analysis and Amy Brice (Colorado School of Mines) for editorial assistance.

References

[1] K. Gall, H. J. Maier, Cyclic deformation mechanisms in precipitated NiTi shape memory alloys, Acta Materialia 50 (2002) 4643–4657.

[2] X. Wang, S. Kustov, K. Li, D. Schryvers, B. Verlinden, J. Van Humbeeck, Effect of nanoprecipitates on the transformation behavior and functional properties of a Ti–50.8at.% Ni alloy with micron-sized grains, Acta Materialia 82 (2015) 224–233. doi:10.1016/j.actamat.2014.09.018.

[3] N. Zhou, C. Shen, M. F. X. Wagner, G. Eggeler, M. J. Mills, Y. Wang, Effect of Ni(4)Ti(3) precipitation on martensitic transformation in Ti-Ni, Acta Materialia 58 (2010) 6685–6694. doi:10.1016/j.actamat.2010.08.033.

[4] C. Y. Xie, L. C. Zhao, T. C. Lei, Effect of Ti3ni4 precipitates on the phase transitions in an aged Ti-51.8at% Ni shape memory alloy, Scripta Metallurgica et Materialia 24 (9) (1990) 1753–1758. doi:10.1016/0956-716X(90)90541-N.

[5] C. Efstathiou, H. Sehitoglu, Local transformation strain measurements in precipitated NiTi single crystals, Scripta Materialia 59 (12) (2008) 1263–1266. doi:10.1016/j.scriptamat.2008.08.030.

[6] D. M. Norfleet, P. M. Sarosi, S. Manchiraju, M. F. X. Wagner, M. D. Uchic, P. M. Anderson, M. J. Mills, Transformation-induced plasticity during pseudoelastic deformation in Ni-Ti microcrystals, Acta Materialia 57 (2009) 3549–3561. doi:10.1016/j.actamat.2009.04.009.

[7] H. M. Paranjape, M. L. Bowers, M. J. Mills, P. M. Anderson, Mechanisms for phase transformation induced slip in shape memory alloy micro-crystals, Acta Materialia 132 (2017) 444–454. doi:10.1016/j.actamat.2017.04.066.

[8] M. L. Bowers, X. Chen, M. De Graef, P. M. Anderson, M. J. Mills, Characterization and modeling of defects generated in pseudoelastically deformed NiTi microcrystals, Scripta Materialia 78–79 (2014) 69–72. doi:10.1016/j.scriptamat.2014.02.001.

[9] T. Simon, A. Kroger, C. Somsen, A. Dlouhy, G. Eggeler, On the multiplication of dislocations during martensitic transformations in NiTi shape memory alloys, Acta Materialia 58 (2010) 1850–1860. doi:10.1016/j.actamat.2009.11.028.

[10] H. M. Paranjape, P. P. Paul, H. Sharma, P. Kenesei, J.-S. Park, T. W. Duerig, L. C. Brinson, A. P. Stebner, Influences of granular constraints and surface effects on the heterogeneity of elastic, superelastic, and plastic responses of polycrystalline shape memory alloys, Journal of the Mechanics and Physics of Solids 102 (2017) 46–66. doi:10.1016/j.jmps.2017.02.007.

[11] H. Paranjape, P. M. Anderson, Texture and grain neighborhood effects on Ni–Ti shape memory alloy performance, Modelling and Simulation in Materials Science and Engineering 22 (7) (2014) 075002. doi:10.1088/0965-0393/22/7/075002.

[12] B. Reinholz, S. Brinckmann, Phase transformations in the proximity of TiC precipitates in a NiTi matrix during fatigue, International Journal of Fatigue 41 (2012) 72–82. doi:10.1016/j.ijfatigue.2012.01.017.

[13] S. W. Robertson, A. R. Pelton, R. O. Ritchie, Mechanical fatigue and fracture of Nitinol, International Materials Reviews 57 (1) (2012) 1–37. doi:10.1179/1743280411Y.0000000009.

[14] R. Vaidyanathan, D. C. Dunand, U. Ramamurty, Fatigue crack-growth in shape-memory NiTi and NiTi–TiC composites, Materials Science and Engineering: A 289 (1–2) (2000) 208–216. doi:10.1016/S0921-5093(00)00882-0.

[15] Y. Gao, N. Zhou, F. Yang, Y. Cui, L. Kovarik, N. Hatcher, R. Noebe, M. J. Mills, Y. Wang, P-phase precipitation and its effect on martensitic transformation in (Ni,Pt)Ti shape memory alloys, Acta Materialia 60 (4) (2012) 1514–1527. doi:10.1016/j.actamat.2011.11.043.

[16] S. M. Ueland, C. A. Schuh, Grain boundary and triple junction constraints during martensitic transformation in shape memory alloys, Journal of Applied Physics 114 (5) (2013) 053503. doi:10.1063/1.4817170.

[17] M. Kimiecik, J. W. Jones, S. Daly, The effect of microstructure on stress-induced martensitic transformation under cyclic loading in the SMA Nickel-Titanium, Journal of the Mechanics and Physics of Solids 89 (2016) 16–30. doi:10.1016/j.jmps.2016.01.007.

[18] T. J. Turner, P. A. Shade, J. V. Bernier, S. F. Li, J. C. Schuren, P. Kenesei, R. M. Suter, J. Almer, Crystal Plasticity Model Validation Using Combined High-Energy Diffraction Microscopy Data for a Ti-7al Specimen, Metallurgical and Materials Transactions A (2016) 1–21doi:10.1007/s11661-016-3868-x.

[19] S. A. Chester, J. V. Bernier, N. R. Barton, L. Balogh, B. Clausen, J. K. Edmiston,

Direct numerical simulation of deformation twinning in polycrystals, Acta Materialia 120 (2016) 348–363. doi:10.1016/j.actamat.2016.08.054.

[20] D. C. Pagan, P. A. Shade, N. R. Barton, J.-S. Park, P. Kenesei, D. B. Menasche, J. V. Bernier, Modeling slip system strength evolution in Ti-7al informed by in-situ grain stress measurements, Acta Materialia 128 (2017) 406–417. doi:10.1016/j.actamat.2017.02.042.

[21] J. C. Schuren, S. L. Wong, P. R. Dawson, M. P. Miller, Integrating experiments and simulations to estimate uncertainty in lattice strain measurements, The Journal of Strain Analysis for Engineering Design 49 (1) (2014) 33–50. doi:10.1177/0309324713492325.

[22] M. P. Miller, P. R. Dawson, Understanding local deformation in metallic polycrystals using high energy X-rays and finite elements, Current Opinion in Solid State and Materials Sciencedoi:10.1016/j.cossms.2014.09.001.

[23] M. Obstalecki, S. L. Wong, P. R. Dawson, M. P. Miller, Quantitative analysis of crystal scale deformation heterogeneity during cyclic plasticity using high-energy X-ray diffraction and finite-element simulation, Acta Materialia 75 (2014) 259–272. doi:10.1016/j.actamat.2014.04.059.

[24] S. L. Wong, M. Obstalecki, M. P. Miller, P. R. Dawson, Stress and deformation heterogeneity in individual grains within polycrystals subjected to fully reversed cyclic loading, Journal of the Mechanics and Physics of Solids 79 (2015) 157–185. doi:10.1016/j.jmps.2015.03.010.

[25] J.-S. Park, A. K. Ray, P. R. Dawson, U. Lienert, M. P. Miller, Determination of residual stress in a microtextured titanium component using high-energy synchrotron X-rays, The Journal of Strain Analysis for Engineering Design 51 (5) (2016) 358–374. doi:10.1177/0309324716640419.

[26] R. Carson, M. Obstalecki, M. Miller, P. R. Dawson, Characterizing Heterogeneous Intragranular Deformations in Polycrystalline Solids Using Diffraction-Based and Mechanics-Based Metrics, Modelling and Simulation in Materials Science and Engineeringdoi:10.1088/1361-651X/aa6dc5.

[27] S. Berveiller, B. Malard, J. Wright, E. Patoor, G. Geandier, In situ synchrotron analysis of lattice rotations in individual grains during stress-induced martensitic transformations in a polycrystalline CuAlBe shape memory alloy, Acta Materialia 59 (9) (2011) 3636–3645. doi:10.1016/j.actamat.2011.02.037.

[28] P. Sedmák, J. Pilch, L. Heller, J. Kopeček, J. Wright, P. Sedlák, M. Frost, P. Šittner, Grain-resolved analysis of localized deformation in nickel-titanium wire under tensile load, Science 353 (6299) (2016) 559–562. doi:10.1126/science.aad6700.

[29] P. A. Shade, B. Blank, J. C. Schuren, T. J. Turner, P. Kenesei, K. Goetze, R. M. Suter, J. V. Bernier, S. F. Li, J. Lind, U. Lienert, J. Almer, A rotational and axial motion system load frame insert for in situ high energy x-ray studies, Review of Scientific Instruments 86 (9) (2015) 093902. doi:10.1063/1.4927855.

[30] J. V. Bernier, N. R. Barton, U. Lienert, M. P. Miller, Far-field high-energy diffraction microscopy: a tool for intergranular orientation and strain analysis, The Journal of Strain Analysis for Engineering Design (2011) 0309324711405761doi:10.1177/0309324711405761.

[31] J. C. Schuren, P. A. Shade, J. V. Bernier, S. F. Li, B. Blank, J. Lind, P. Kenesei, U. Lienert, R. M. Suter, T. J. Turner, D. M. Dimiduk, J. Almer, New opportunities for quantitative tracking of polycrystal responses in three dimensions, Current Opinion in Solid State and Materials Science 19 (4) (2015) 235–244. doi:10.1016/j.cossms.2014.11.003.

[32] H. Sharma, R. M. Huizenga, A. Bytchkov, J. Sietsma, S. E. Offerman, Observation of changing crystal orientations during grain coarsening, Acta Materialia 60 (1) (2012) 229–237. doi:10.1016/j.actamat.2011.09.057.

[33] H. Sharma, R. M. Huizenga, S. E. Offerman, A fast methodology to determine the characteristics of thousands of grains using three-dimensional X-ray diffraction. I. Overlapping diffraction peaks and parameters of the experimental setup, Journal of Applied Crystallography 45 (4) (2012) 693–704. doi:10.1107/S0021889812025563.

[34] H. Sharma, R. M. Huizenga, S. E. Offerman, A fast methodology to determine the characteristics of thousands of grains using three-dimensional X-ray diffraction. II. Volume, centre-of-mass position, crystallographic orientation and strain state of grains, Journal of Applied Crystallography 45 (4) (2012) 705–718. doi:10.1107/S0021889812025599.

[35] U. Lienert, S. F. Li, C. M. Hefferan, J. Lind, R. M. Suter, J. V. Bernier, N. R. Barton, M. C. Brandes, M. J. Mills, M. P. Miller, B. Jakobsen, W. Pantleon, High-energy diffraction microscopy at the advanced photon source, Jom 63 (2011) 70–77. doi:10.1007/s11837-011-0116-0.

[36] J. H. Lee, C. C. Aydner, J. Almer, J. Bernier, K. W. Chapman, P. J. Chupas, D. Haeffner, K. Kump, P. L. Lee, U. Lienert, A. Miceli, G. Vera, Synchrotron applications of an amorphous silicon flat-panel detector, Journal of Synchrotron Radiation 15 (5) (2008) 477–488. doi:10.1107/S090904950801755X.

[37] H. Sharma, J. Almer, J. S. Park, P. Kenesei, M. Wilde, J. Wozniak, MIDAS, Microstructural Imaging using Diffraction Analysis Software (2016).
URL `https://www1.aps.anl.gov/science/scientific-software/midas`

[38] H. Paranjape, Mechanicsnext: Mechanics of materials using numerical and experimental techniques, https://github.com/MechanicsNext/MechanicsNext (2017). doi:10.5281/zenodo.822831.
URL https://github.com/MechanicsNext/MechanicsNext

[39] HEXRD Developers, HEXRD: A collection of resources for analysis of x-ray diffraction data, especially high-energy x-ray diffraction.
URL https://github.com/praxes/hexrd

[40] C. Bewerse, K. R. Gall, G. J. McFarland, P. Zhu, L. C. Brinson, Local and global strains and strain ratios in shape memory alloys using digital image correlation, Materials Science and Engineering: A 568 (2013) 134–142. doi:10.1016/j.msea.2013.01.030.

[41] S. Daly, G. Ravichandran, K. Bhattacharya, Stress-induced martensitic phase transformation in thin sheets of Nitinol, Acta Materialia 55 (2007) 3593–3600. doi:10.1016/j.actamat.2007.02.011.

[42] K. Kim, S. Daly, Martensite Strain Memory in the Shape Memory Alloy Nickel-Titanium Under Mechanical Cycling, Experimental Mechanics 51 (2011) 641–652. doi:10.1007/s11340-010-9435-2.

[43] J. Blaber, B. Adair, A. Antoniou, Ncorr: Open-Source 2d Digital Image Correlation Matlab Software, Experimental Mechanics 55 (6) (2015) 1105–1122. doi:10.1007/s11340-015-0009-1.

[44] H. Sehitoglu, I. Karaman, R. Anderson, X. Zhang, K. Gall, H. J. Maier, Y. Chumlyakov, Compressive response of NiTi single crystals, Acta Materialia 48 (13) (2000) 3311–3326.

[45] F. Bachmann, R. Hielscher, H. Schaeben, Texture Analysis with MTEX – Free and Open Source Software Toolbox, Solid State Phenomena 160 (2010) 63–68. doi:10.4028/www.scientific.net/SSP.160.63.

[46] K. Bhattacharya, Microstructure of Martensite: Why it forms and how it gives rise to the shape-memory effect, Oxford University Press, 2003.

[47] ABAQUS, Abaqus Reference Manuals.

[48] J. Frenzel, Z. Zhang, C. Somsen, K. Neuking, G. Eggeler, Influence of carbon on martensitic phase transformations in NiTi shape memory alloys, Acta Materialia 55 (4) (2007) 1331–1341. doi:10.1016/j.actamat.2006.10.006.

[49] M. Rahim, J. Frenzel, M. Frotscher, J. Pfetzing-Micklich, R. Steegmüller, M. Wohlschlögel, H. Mughrabi, G. Eggeler, Impurity levels and fatigue lives of pseudoelastic NiTi shape memory alloys, Acta Materialia 61 (10) (2013) 3667–3686. doi:10.1016/j.actamat.2013.02.054.

[50] J. Michutta, C. Somsen, A. Yawny, A. Dlouhy, G. Eggeler, Elementary martensitic

transformation processes in Ni-rich NiTi single crystals with Ni4ti3 precipitates, Acta Materialia 54 (13) (2006) 3525–3542. doi:10.1016/j.actamat.2006.03.036.

[51] T. Merzouki, C. Collard, N. Bourgeois, T. Ben Zineb, F. Meraghni, Coupling between measured kinematic fields and multicrystal SMA finite element calculations, Mechanics of Materials 42 (1) (2010) 72–95. doi:10.1016/j.mechmat.2009.09.003.

[52] X. Y. Zhang, L. C. Brinson, Q. P. Sun, The variant selection criteria in single-crystal CuAlNi shape memory alloys, Smart materials and structures 9 (5) (2000) 571.

[53] O. Matsumoto, S. Miyazaki, K. Otsuka, H. Tamura, Crystallography of martensitic transformation in Ti-Ni single crystals, Acta Metallurgica 35 (8) (1987) 2137–2144. doi:10.1016/0001-6160(87)90042-3.

[54] X. Balandraud, N. Barrera, P. Biscari, M. Grédiac, G. Zanzotto, Strain intermittency in shape-memory alloys, Physical Review B 91 (17). doi:10.1103/PhysRevB.91.174111.

[55] W. Tirry, D. Schryvers, Quantitative determination of strain fields around Ni4ti3 precipitates in NiTi, Acta Materialia 53 (4) (2005) 1041–1049. doi:10.1016/j.actamat.2004.10.049.

[56] W. Tirry, D. Schryvers, Linking a completely three-dimensional nanostrain to a structural transformation eigenstrain, Nature Materials 8 (9) (2009) 752–757. doi:10.1038/nmat2488.

[57] S. Miyazaki, K. Otsuka, Deformation and transition behavior associated with the r-phase in ti-ni alloys, Metallurgical Transactions a-Physical Metallurgy and Materials Science 17 (1986) 53–63. doi:10.1007/bf02644442.

[58] S. Miyazaki, C. M. Wayman, The R-phase transition and associated shape memory mechanism in Ti-Ni single crystals, Acta Metallurgica 36 (1) (1988) 181–192. doi:10.1016/0001-6160(88)90037-5.

[59] A. Dlouhy, J. Khalil-Allafi, G. Eggeler, Multiple-step martensitic transformations in Ni-rich NiTi alloys–an in-situ transmission electron microscopy investigation, Philosophical Magazine 83 (3) (2003) 339–363. doi:10.1080/0141861021000034531.

[60] P. Lukas, P. Sittner, D. Lugovoy, D. Neov, M. Ceretti, In situ neutron diffraction studies of the R-phase transformation in the NiTi shape memory alloy, Applied Physics A: Materials Science & Processing 74 (0) (2002) s1121–s1123. doi:10.1007/s003390101201.

[61] P. Šittner, M. Landa, P. Lukáš, V. Novák, R-phase transformation phenomena in thermomechanically loaded NiTi polycrystals, Mechanics of Materials 38 (5–6) (2006) 475–492. doi:10.1016/j.mechmat.2005.05.025.

[62] X. Zhang, H. Sehitoglu, Crystallography of the B2 R B19 phase transforma-

tions in NiTi, Materials Science and Engineering: A 374 (1-2) (2004) 292–302. doi:10.1016/j.msea.2004.03.013.

[63] R. D. Dar, H. Yan, Y. Chen, Grain boundary engineering of Co–Ni–Al, Cu–Zn–Al, and Cu–Al–Ni shape memory alloys by intergranular precipitation of a ductile solid solution phase, Scripta Materialia 115 (2016) 113–117. doi:10.1016/j.scriptamat.2016.01.014.

[64] X. Li, K. Lu, Playing with defects in metals, Nat Mater 16 (7) (2017) 700–701.